Calibration for Circular Cone-Beam CT Based on Consistency Conditions

Jérôme Lesaint, Simon Rit, Rolf Clackdoyle, and Laurent Desbat

***Abstract*—In cone-beam computed tomography (CT), imprecise knowledge of the acquisition geometry can severely impact the quality of the reconstructed image. This paper investigates geometric calibration using data consistency conditions (DCCs). Unlike the usual marker-based off-line methods, the proposed method does not require the extra-scan of a calibration phantom. It is based on the minimization of a cost function, which measures the inconsistency between pairs of projections. The method has been applied to both simulated and real data. The latter were acquired from a micro-CT system with circular trajectory, for which the problem reduces to identifying global misalignments of the system. When compared to uncorrected reconstruction, the method significantly improved the image quality. When compared to marker-based calibration method, the image quality was similar but no calibration scan was required. Finally, the method can handle axially truncated data. Axial truncation is very common in the medical context but often considered intractable for DCC-based methods. We also demonstrate DCC calibration from real data with axial truncation.**

***Index Terms*—Cone-beam computed tomography (CBCT), data consistency conditions (DCCs), geometric calibration, micro-CT.**

I. Introduction

In CONE-BEAM computed tomography (CBCT), a 3-D image is reconstructed from a set of 2-D projections acquired from a point-like X-ray source. Poor reconstructed image quality can arise due to many possible causes. One of these causes is an inaccurate calibration of the system. Calibration is the process through which the geometry of acquisition of the projections is accurately determined. By geometry of acquisition, we mean the position and orientation of the detector and the position of the X-ray source in a fixed reference frame.

Calibration of a CBCT system has been studied for a long time. Early works used the scan of a dedicated phantom to estimate the geometric parameters. These are known as *off-line* methods, to emphasize the need for a preliminary scan. The calibration scan provides accurate geometry information as long as the misalignments that were estimated are reproducible over time. In the extreme case, where mechanical flexibility of the system makes the reproducibility assumption false, these methods become invalid. More recently, *on-line* (or *self-*) calibration methods have been developed. For each acquisition, and before reconstruction, the calibration is computed directly from the projections.

This paper presents an *on-line* method based on the minimization of a cost function, that quantifies the inconsistency of the set of measured projections. The data consistency conditions (DCCs) that are incorporated in the cost function have been described in many different works (see Section II-C). They are essentially fan-beam consistency conditions for a linear trajectory. They have been adapted to a circular trajectory CBCT system by resampling each pair of projections into a virtual detector parallel to the line connecting pairs of source positions. This idea was already proposed in [1] but, to the best of our knowledge, never implemented or applied to any CT reconstruction problem. This paper is very similar in its geometric approach to other recent works [2], [3] but differs fundamentally in the DCCs which are used. The proposed method was applied to simulated and real data, and compared with a robust *off-line* method.

II. Notation and Background

The micro-CT system to which the calibration method was applied is made of a 2-D flat detector and a fixed X-ray source. A turntable placed between the two allowed a full 360° rotation of the object (see Fig. 1), so the acquisition geometry was equivalent to a circular trajectory of the source and detector. We will describe the geometry in detail, together with the calibration parameters that we are trying to estimate.

A. Description of the Geometry

We use the same geometric description as that given in [4]. The detector cells are perfect squares (same width and height, arranged on a Cartesian grid). Let (x, y, z) be a fixed reference frame, defined as follows: the y-axis is the axis of rotation of the turntable. The origin is set so that the source lies in the $y = 0$ plane. The z-axis contains the source at rotation angle 0 and points in the direction of the source. The x-axis is defined so that (x, y, z) is a right-handed coordinate system. The flat panel detector is equipped with a direct

Manuscript received April 18, 2017; revised July 4, 2017; accepted July 28, 2017. Date of publication August 1, 2017; date of current version November 1, 2017. This work was supported by the Agence Nationale de la Recherche, France, under Grant Labex CAMI ANR-11-LABX-0004-01, Grant Labex PRIMES ANR-11-LABX-0063, and Project DROITE ANR-12-BS01-0018. *(Corresponding author: Jérôme Lesaint.)*

J. Lesaint, R. Clackdoyle, and L. Desbat are with the TIMC-IMAG Laboratory, CNRS UMR 5525, Université Grenoble Alpes, 38707 La Tronche, France (e-mail: jerome.lesaint@univ-grenoble-alpes.fr).

S. Rit is with Univ. Lyon, INSA-Lyon, UCB Lyon 1, UJM-Saint Etienne, CNRS, Inserm, CREATIS UMR5220, U1206, Centre Léon Bérard, F-69373 Lyon, France.

Color versions of one or more of the figures in this paper are available online at http://ieeexplore.ieee.org.

Digital Object Identifier 10.1109/TRPMS.2017.2734844

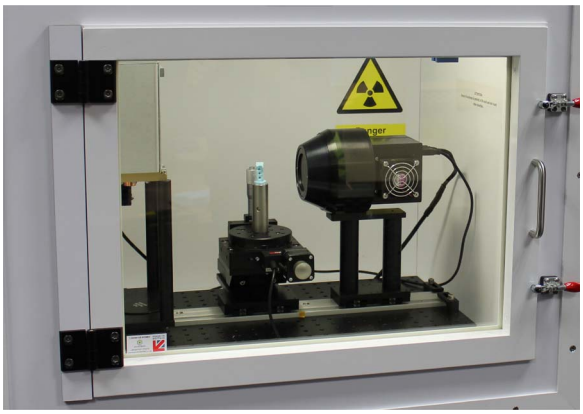

Fig. 1. Picture of the CT system. Source (left) is fixed. Turntable (middle) and detector (right) are adjustable. Detector size: 35 × 35 mm. Pixel size: 17.09 μm.

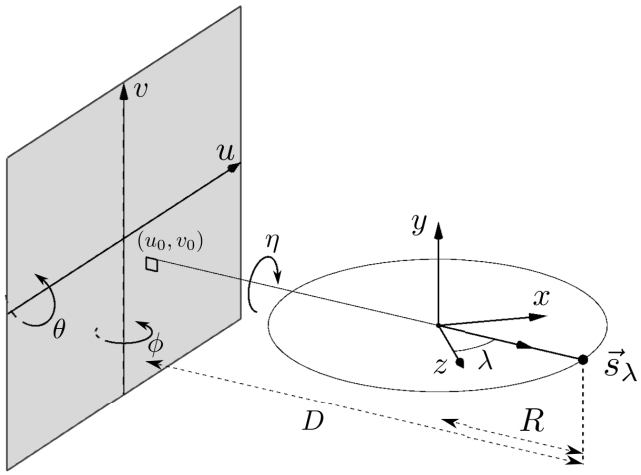

Fig. 2. Illustration of the eight geometric parameters. The detector orientation is defined by three Euler angles. η is the in-plane angle. ϕ and θ are out-of-plane rotations about the v-axis and the u-axis, respectively.

(u, v) coordinate system whose origin is the center of the detector and whose axes coincide with the pixel rows and columns, respectively. The geometry of one projection can be unambiguously described with eight parameters (see Fig. 2).

- The rotation angle λ, taken from the z-axis.
- The radius of the source trajectory R.
- Three orientation angles of the detector (ϕ, θ, η).
- The source to detector distance D (or focal distance).
- The coordinates (u_0, v_0) of the principal point (orthogonal projection of the source onto the detector plane).

With this parametrization, for $\lambda \in [0; 2\pi[$, the source position is given by $\vec{s}_\lambda = (R\sin\lambda, 0, R\cos\lambda)$. The orientation of the detector is described with three Euler angles η, θ, and ϕ (called *yaw, pitch, roll*, respectively, in [5] and *skew, tilt, slant* in [6]) applied in this order (respective axes of rotations are illustrated in Fig. 2). The normal to the detector is defined with two out-of-plane angles θ and ϕ about the u- and v-axes, respectively. The in-plane rotation (about the focal axis) is given by η. The circular geometry thus consists of 8 degrees-of-freedom, unless the relative position and orientation

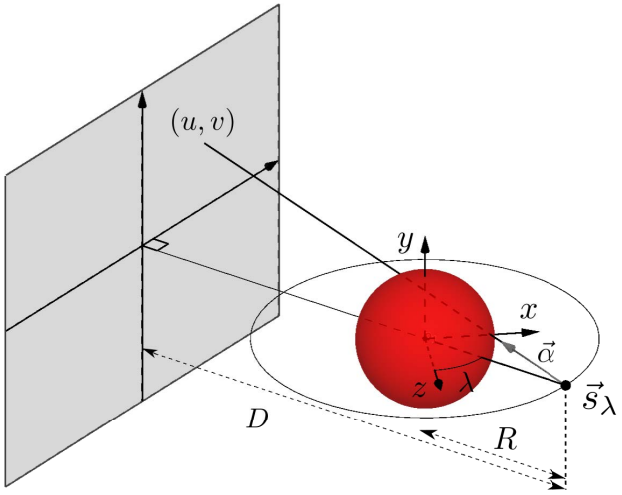

Fig. 3. Cone-beam geometry with circular trajectory. For a given scalar λ (typically in $[0, 2\pi]$), $\vec{s}_\lambda$ denotes the position of the source. $\vec{\alpha}$ is a unit 3-D vector ($\in \mathcal{S}^2$) that gives the direction of one X-ray. Note here that the system is *perfectly aligned*: the v-axis is parallel to the rotation y-axis ($\theta = \eta = 0$). The u-axis is perpendicular to the direction of the source ($\phi = 0$) and the detector is not shifted ($u_0 = v_0 = 0$).

of the source and detector can vary across projections. In our micro-CT system, the source and the detector are fixed, so the only projection-specific parameter is the rotation angle. The other seven parameters remain constant through the acquisition cycle. We call these parameters *global misalignment parameters* or *global geometric parameters* and refer to the corresponding geometry as *true geometry*. The system is *perfectly aligned* when (1) the principal axis (orthogonal to the detector plane and passing through the source) contains both the world origin and the detector origin and (2) the u and v axes of the detector are parallel to the x and y axes of the world frame at rotation angle $\lambda = 0$. In terms of the geometric parameters, these two conditions are equivalent to $\theta = \phi = \eta = u_0 = v_0 = 0$. We refer to the corresponding geometry as *nominal geometry*.

B. X-Ray Line-Integral Model

If $f(\vec{x}) = f(x, y, z)$ denotes the object density function, the projection $g(\lambda, \cdot)$ is defined by the usual line integral model

$$g(\lambda, \vec{\alpha}) = \int_0^\infty f(\vec{s}_\lambda + t\vec{\alpha})\mathrm{d}t, \quad \forall \vec{\alpha} \in \mathcal{S}^2 \tag{1}$$

where $\mathcal{S}^2$ denotes the unit-sphere of $\mathbb{R}^3$. The projection $g(\lambda, \cdot)$ vanishes for all $\vec{\alpha}$ such that the line originating at $\vec{s}_\lambda$ and directed by $\vec{\alpha}$ does not intersect the support of f (see Fig. 3).

C. Review of Existing Calibration Methods

Much work has been done on the calibration of CT systems. We give a quick review of the methods and briefly summarize the relative importance of each parameter with respect to their impact on the reconstruction quality. If N denotes the number of acquired projections, the most general calibration problem consists of estimating—for each projection—the eleven independent coefficients of the 3×4 projection matrix

in homogeneous coordinates (see [7]). If the detector rows and columns are known to be perpendicular with the same sampling in both directions (i.e., square pixels) then two degrees of freedom are eliminated and the task reduces to estimating nine projection-specific geometric parameters (three for the source position, three for the detector position, and another three for the orientation of the gantry). As described in the previous section, the circular trajectory we are considering in this paper is completely described by seven global geometric parameters. The only projection-specific parameter is the rotation angle.

Imaging-based calibration methods fall into two broad categories. One category consists of the off-line methods [4]–[6], [8]–[12]: they all require prescanning of a calibration phantom, usually made up of small ball bearings (BBs) whose relative positions are accurately known. Then the theoretical projections of the BBs (which depend on the geometric parameters) are compared with their actual projections to derive—iteratively [8], [9] or analytically [4]–[6], [10]–[12]—the calibration parameters. In [12], they solve the complete calibration problem and analytically derive all nine parameters for each projection.

The other group of techniques consists of *on-line* techniques. All methods in this category solve the calibration problem without a specific calibration scan of a calibration object. They only use the data from the projections of the imaged object. Beyond this common feature, this group encompasses substantially different techniques. In [13]–[15], they minimize a cost function, whose evaluation requires the reconstruction of the object from the current estimate of the geometric parameters. The metric is based on entropy in [13], the L^2-norm of the image gradient in [14] or the mutual information between reprojected image and projection data in [15]. The limitation of such methods is the computational load, which may not fit clinical workflow (though [14] limits this drawback by only reconstructing a fraction of the volume). In [16], they use the 3-D reconstruction of a planning CT and compute projection-specific geometric parameters by registering the actual projections with the reprojected CT image. Other works in this category utilize the redundancy of the projection data (i.e., the DCCs). In the 2-D parallel beam case, Basu and Bresler [17], [18] solved uniquely and efficiently the problem of unknown projection angles and shifts with the Helgason–Ludwig DCCs. Some works use the trivial "opposite-ray" condition [19]–[21]. In [19], this DCC, which normally only applies in the central plane (the plane of the trajectory), is extended to cone-beam projections of a particular class of symmetric 3-D object functions and shows accurate calibration results when approximated in a central region of a generic object. More closely related to this paper is a series of publications on epipolar consistency conditions (ECCs) [2], [3], [22]. These DCCs are based on the Grangeat theorem and relate the derivative of the 2-D Radon transform of the projections to the derivative of the 3-D Radon transform of the imaged object.

The comparison of previous works is not easy due to the parametrization which may differ with authors. Nevertheless, it is widely documented that the detector shift u_0 and the in-plane angle η are of crucial importance [4]–[6], [11]. On the other hand, [11], [15] demonstrated that the two out-of-plane angles (ϕ and θ) may be set to zero without affecting the image quality if their true values are kept below 2° (which is a reasonable manufacturing accuracy requirement). Finally, miscalibration of the source-to-center and source-to-detector distances does not introduce artifacts in the reconstructed volume and are therefore not calibrated. However, these two parameters affect the magnification of the reconstructed volume, which would not be acceptable in some cases, such as a metrology-oriented application.

III. Methods

A. Cone-Beam DCCs for Linear Trajectory

DCCs are conditions which must be satisfied by the projection data in order for them to be the image of an object function through the forward projection model described in (1). DCCs have been applied to various CT artefact correction techniques, e.g., motion compensation [23]–[25] and beam hardening correction [26]. The simplest condition is the "opposite-ray condition." In parallel projection geometry, it states that the projections must be even: $\mathcal{R}f(\vec{\alpha}, s) = \mathcal{R}f(-\vec{\alpha}, -s)$, where $\mathcal{R}f$ denotes the 2-D Radon transform of an object function f. This condition was applied to the calibration problem in [19]. Still in the parallel geometry, there exists a complete set of DCCs, known as Helgason–Ludwig DCCs (see [27], [28] and standard textbooks on the Radon transform, e.g., [29] and [30]), which relates the nth order moments of each projection to a homogeneous polynomial of order n. In the 2-D divergent geometry (fan-beam projections), complete DCCs, similar to Helgason–Ludwig polynomial conditions, were derived in [31] for the particular case of an X-ray source moving along a line. We will be using the order-0 case, which was known much earlier than the latter work (see their various guises in [32]–[36] for a review).

The description of cone-beam pair-wise consistency conditions follows [1]. Let $\vec{s}_{\lambda_i}$ and $\vec{s}_{\lambda_j}$ be two source positions and $L_{i,j}$ be the line connecting them. Suppose that both projections are acquired with one common flat detector, parallel to $L_{i,j}$. Any plane containing $L_{i,j}$ intersects—if it does—the detector on a row, parallel to $L_{i,j}$, which we will index with k. We will denote that plane $P_{i,j,k}$. The situation in $P_{i,j,k}$ reduces to a pair of fan-beam projections along the virtual linear trajectory $L_{i,j}$ and with the kth detector row playing the role of the 1-D fan-beam detector. The order-0 DCCs state the following.

Lemma 1: For any pair of projection indices i, j and any integer k, let

$$G_{i,j,k} = \int_{-\frac{\pi}{2}}^{\frac{\pi}{2}} \frac{g\left(\lambda_i, \vec{\alpha}_\phi^k\right)}{\cos\phi} d\phi \tag{2}$$

where $\vec{\alpha}_\phi^k$ denotes a unit vector in $P_{i,j,k}$, ϕ denotes the angle between $\vec{\alpha}_\phi^k$ and the perpendicular to $L_{i,j}$ in that plane. Furthermore, the line $L_{i,j}$ is assumed to not intersect the support of the object function f. See Figs. 4 and 5.

If the data are consistent, then

$$G_{i,j,k} - G_{j,i,k} = 0 \tag{3}$$

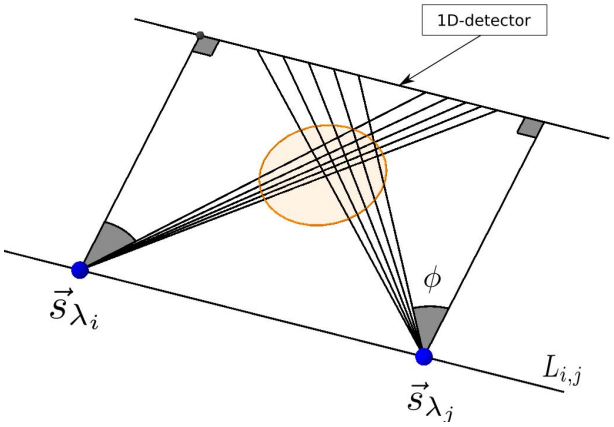

Fig. 4. View of one plane $P_{i,j,k}$. Order-0 fan-beam DCCs state that the integral of the cosine-weighted projections are equal.

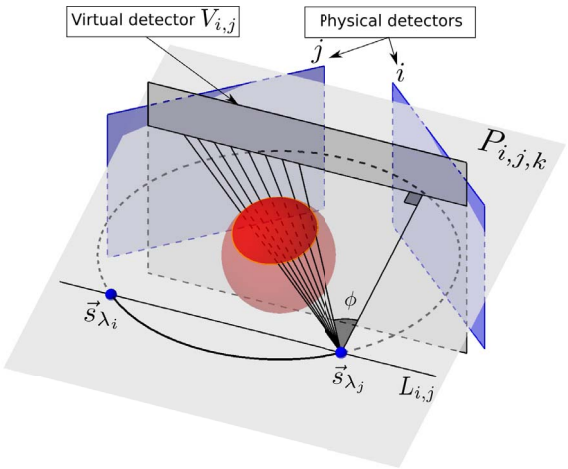

Fig. 5. Two sources on a circular trajectory. Both projections are backprojected in a virtual detector, parallel to the line connecting $\vec{s}_{\lambda_i}$ and $\vec{s}_{\lambda_j}$.

Let $c_{i,j,k}$ denote the square difference of the left-hand side of (3). The sum $C_{i,j} = \sum_k c_{i,j,k}$ is a measure of the pair-wise consistency between two cone-beam projections $g(\lambda_i, \cdot)$ and $g(\lambda_j, \cdot)$.

B. Resampling in Virtual Detector

These DCCs only apply if the detector is parallel to the virtual linear trajectory $L_{i,j}$ connecting two source positions. In the circular trajectory we are considering in this paper, this detector condition is obviously not fulfilled. To remedy this problem, each pair of projections is resampled onto a virtual detector $V_{i,j}$ by means of a backprojection. The virtual detector is placed at the origin of the world system of coordinates and oriented in such a way that the rows and columns of $V_{i,j}$ are parallel to $L_{i,j}$ and the axis of rotation, respectively. The situation is illustrated in Fig. 5.

The orientation of the virtual detector allows a simple evaluation of the integral $G_{i,j,k}$ in (2) by changing the ϕ-variable to the u-pixel coordinate of the virtual detector with

$$u = \sqrt{v_k^2 + D_{\text{virt}}^2} \tan \phi$$

Algorithm 1 Pseudo-Code for the Cost Function

```
procedure COST(p)
    Initalize C = 0
    for Each pair of sources (i, j) ∈ Ω: do
        Backproject projections onto V_{i,j}.
        Pre-weight the virtual projections acc. to Eq. 4.
        for Each row k: do
            Compute the line integrals G_{i,j,k} and G_{j,i,k}.
            Compute the squared difference c_{i,j,k}.
            Add to C.
        end for
    end for
end procedure
```

where v_k is the intercept of the plane $P_{i,j,k}$ with the virtual detector's v-axis and D_{virt} denotes the distance from the source to the virtual detector. Applying this change of variables leads to

$$G_{i,j,k} = \frac{1}{\sqrt{v_k^2 + D_{\text{virt}}^2}} \int_{\mathbb{R}} g(\lambda_i, u) \frac{\sqrt{v_k^2 + D_{\text{virt}}^2}}{\sqrt{u^2 + v_k^2 + D^2}} du. \quad (4)$$

Note that the weight inside the integral is exactly $\cos\phi$. The change of variables has moved this cosine term from the denominator to the numerator.

When applying these DCCs to the calibration problem, we note that the backprojection onto the virtual detector will use the projection geometry as input. Hence, the dependency of the cost function (described in the next section) on the calibration parameters via this backprojection.

C. Consistency Metric

Estimation of the geometric calibration parameters is achieved by minimizing a cost function based on the pair-wise consistency conditions described above. Let $\mathbf{p} = (\phi, \theta, \eta, u_0, v_0, R, D)$ denote the 7-uple of sought parameters. We define the cost function $C(\mathbf{p})$ as follows:

$$C(\mathbf{p}) = \sum_{(i,j)\in\Omega} C_{i,j} = \sum_{(i,j)\in\Omega} \sum_k c_{i,j,k} \quad (5)$$

where $C_{i,j}$ was defined above with the dependence on $\mathbf{p}$ buried in the backprojection onto the virtual detector, Ω is the chosen subset of pairs of projections to which the DCCs are applied.

The size of the virtual detector $V_{i,j}$ is computed to account for the distortion resulting from the backprojection step (see details is Section V-C1). For each pair of projections, the cost function is evaluated over all rows k of $V_{i,j}$.

The computation of the cost function can be summarized in Algorithm 1.

IV. Numerical Experiments on Simulated Data

We first studied the properties of our cost function on simulated projections of a Shepp–Logan phantom and estimated the accuracy that can be expected from our method. All simulated projection data were generated with the reconstruction

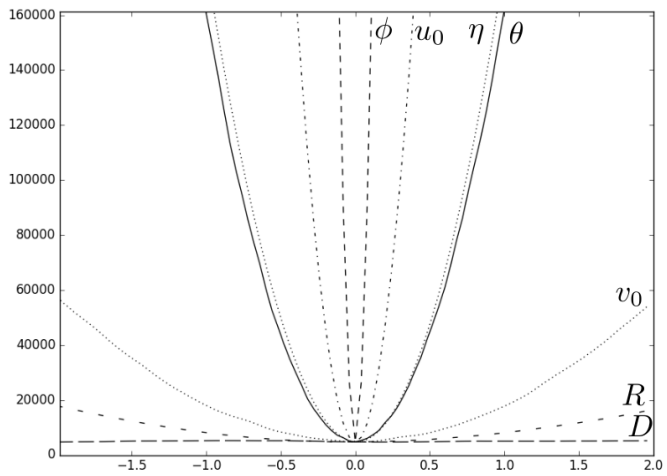

Fig. 6. Cost function as a 1-D function of each estimated parameter, evaluated on the simulated projection data of a standard Shepp–Logan phantom. 90 equally spaced projections were simulated over a full 360° circular acquisition. For each parameter, the cost function is evaluated at 50 equally-spaced parameter values, ranging from −2 to 2. Note that the minimum function value is not zero due to numerical errors.

toolkit (RTK) software package [37]. All reconstructions were computed with the Feldkamp algorithm [38] available in RTK.

In all our experiments, the set Ω was composed of 27 projections pairs, constructed as follows: nine equally spaced projections (spaced by 40°) were selected and all possible pairs were included in Ω, except those separated by $\pm 160°$. This particular choice for Ω arose from a tradeoff between the computational load and the amount of data we inject in the cost function for robust parameter estimation. Pairs separated by $\pm 160°$ were removed because they are too close to the limit situation where the line $L_{i,j}$ (hence the virtual detector) would be perpendicular to the physical detectors. Also, the maximum separation of the remaining pairs was 120° which eliminated any risk of the connecting line intersecting the scanned object.

A. Cost Function Study

We first studied the behavior of our cost function on the simulated projections of a 3-D Shepp–Logan phantom [39]. Projections were simulated with a *perfectly aligned* system ($R = 100$, $D = 200$ and all other geometric parameters set to zero). Then, we computed the cost function as a 1-D-function of each separate parameter, over a symmetric interval $[-2, 2]$ (in degrees for η, θ, and ϕ and in millimeters for u_0, v_0, R, and D). Fig. 6 shows corresponding plots. Note that the cost function has very low dependence on the two distances R and D. For this reason, these two parameters will not be optimized in our calibration method. Our procedure focuses on the remaining five global parameters. The plots in Fig. 6 indicate that the cost function is locally convex with respect to each of them. The convexity of the 1-D-functions does not guarantee the convexity of the multidimensional cost function but is still encouraging for the optimization procedure to find a suitable minimum. Of the five parameters, the vertical shift v_0 shows the least sensitivity to the DCCs. This fact has a direct effect on the errors we obtained with simulated data (see section below).

TABLE I
RESULTS ON SIMULATED DATA

	η in deg.	θ in deg.	ϕ in deg.	u_0 in mm.	v_0 in mm.
True geometry	0.1	0.2	0.3	0.4	0.5
Exp. 1 (init.: nominal geom.)					
Estimated geometry	0.1040	0.5279	0.3168	0.3540	1.4037
Absolute error	*0.0039*	*0.3279*	*0.0168*	*0.0460*	*0.9037*
Exp. 2 (random init.)					
Mean	0.0975	1.4801	0.2934	0.4198	2.6613
Std	0.0040	1.4834	0.0360	0.1030	4.1100
Absolute mean error	*0.0025*	*1.2801*	*0.0066*	*0.0198*	*2.1613*
Exp. 3 (random init. with fixed $\theta = 0.2$)					
Mean	0.1013	-	0.2862	0.4389	0.4907
Std	0.0008	-	0.0870	0.2471	0.0006
Absolute mean error	*0.0013*	-	*0.0138*	*0.0389*	*0.009*
Exp. 4 (random init. with fixed $v_0 = 0.5$)					
Mean	0.1010	0.2022	0.2857	0.4391	-
Std	0.0009	0.0002	0.0736	0.2101	-
Absolute mean error	*0.0010*	*0.0022*	*0.0143*	*0.0391*	-

B. Calibration on Simulated Data

We applied our calibration method to simulated projections of a 3-D Shepp–Logan phantom. The data were generated using the misalignment parameter values indicated in the first row of Table I. The simulated projections were 256×256 pixels, with pixel size set to 0.25 mm. The source-to-center and source-to-detector distances were set to 100 and 160 mm, respectively. The larger half-length of the outer ellipsoïd of the Shepp–Logan phantom was 15 mm. We used the Numpy implementation of the order-0 minimization method from Powell [40]. Results are recorded in Table I.

In the first experiment (see Exp. 1 in Table I), the calibration procedure was initialized with a *nominal* geometry (all five parameters equal to 0). This initialization corresponds to the best guess we could make on the real μCT system, which is designed to be *perfectly aligned*. In Fig. 7, we present one frontal slice of the 3-D numerical Shepp–Logan phantom (top left). We reconstructed the 3-D volume from the simulated projections data using three different geometries: 1) the true geometry; 2) the DCC-calibrated geometry (resulting from our minimization procedure); and 3) the nominal geometry. The reconstructions are shown in Fig. 7. The reconstruction with the nominal geometry shows severe artifacts (see middle left in Fig. 7) with a root mean square error (RMSE) of 0.311 when compared to the 3-D numerical phantom (top left). No visible difference between the two reconstructions with the true geometry (top right) and with DCC-calibrated geometry (middle right) is apparent. In both cases, the quality of the reconstruction is significantly improved, with RMSE of 0.107 and 0.106, respectively. Note also that the procedure can easily be extended to a short scan trajectory. In the bottom row of Fig. 7, we present a 220° short-scan reconstructions with the nominal geometry (left) and the DCC-calibrated geometry (right). The set Ω was built with nine equally spaced projections over the 220° angular range.

The second experiment focuses on the dependency of the cost function on the initial guess. We ran the procedure with 100 random initial values taken from a normal distribution and computed the mean and standard deviation of each geometric

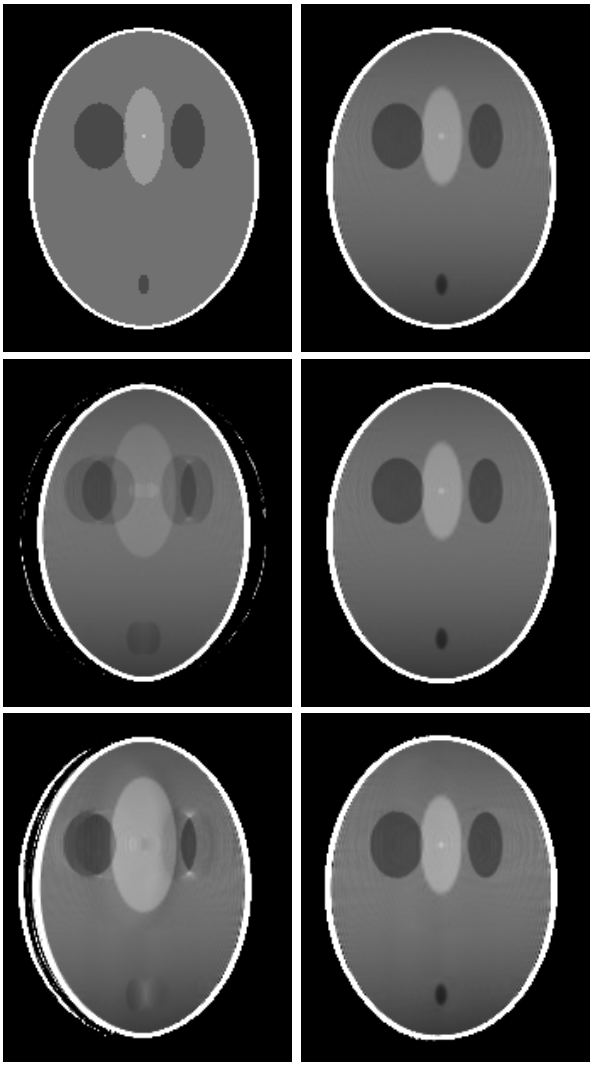

Fig. 7. Top and middle rows: full-scan results. Top left: 3-D Shepp–Logan phantom. Top right: reconstruction with true geometry. Middle left: reconstruction with nominal geometry. Middle right: reconstruction with DCC-calibrated geometry. Bottom left: short scan reconstruction with nominal geometry. Bottom right: short scan reconstruction with DCC-calibrated geometry.

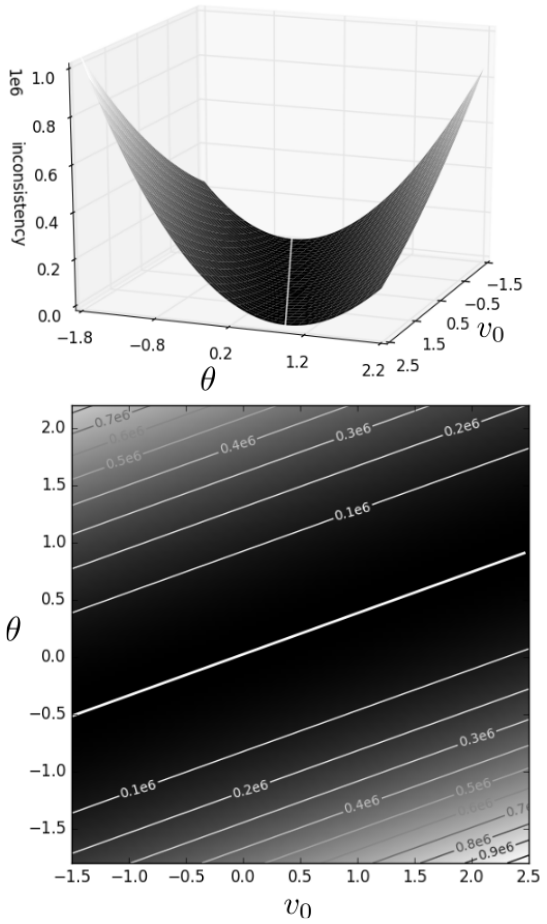

Fig. 8. Consistency metric as a function of θ and v_0 (top: 3-D plot of the function. Bottom: gray-value 2-D map and contour lines). All three others geometric parameters were set to their true values. The white solid line shows the valley along which inconsistency is minimal.

parameter. The results are presented in Table I, Exp. 2. We noticed that the out-of-plane angle θ and the vertical shift of the detector v_0 deviated significantly from their true values (mean errors: 1.28 and 2.16, respectively), with large variability (standard deviations: 1.48 and 4.11, respectively). But this does not affect the quality of the reconstruction as shown in Fig. 7. We observed that the imaged object was well reconstructed but possibly at a slightly different place in space and the reconstruction with DCC-calibrated geometry had to be manually registered on the reference Shepp–Logan by a small translation in the v direction. On the other hand, when one of these two parameters was fixed to its true value, the optimized value of the other was estimated with a high precision and with very low variance (see Table I, Exp. 3, and Exp. 4). This reveals the difficulty of evaluating the quality of a calibration procedure. To better illustrate this compensation phenomenon, we computed the cost function value as a function of θ and v_0 (the other three parameters being fixed to their true values). The plot in Fig. 8 reveals a long flat valley in a direction which is a linear (for small θ) combination of θ and v_0 directions. All the values of θ and v_0 along this valley minimize the cost function and visual inspection of the resulting reconstruction suggested equally good quality.

V. Numerical Experiments on Our μ-CT System

A. Description of the Experimental Set-Up

We applied our method to real data acquired on the micro-CT system depicted in Fig. 1. The X-ray source is fixed. The imaging object is placed on a turntable. The distance between the source and the turntable can be manually adjusted. The source to detector distance can also be manually adjusted, but both distances remain fixed during one complete 360° scan. The detector size is 2048×2048 pixels with pixel size of 17.09^2 μm^2. The X-ray tube voltage was set to 30 kV, the current was set to 0.25 mA and exposure time was set to 2 s. To reduce the computational burden, the projections were down-sampled by a factor of 8 to 256×256 pixels. In each experiment, 360 equally-spaced projections were acquired. Dark-field and flat-field corrections were applied to raw-data.

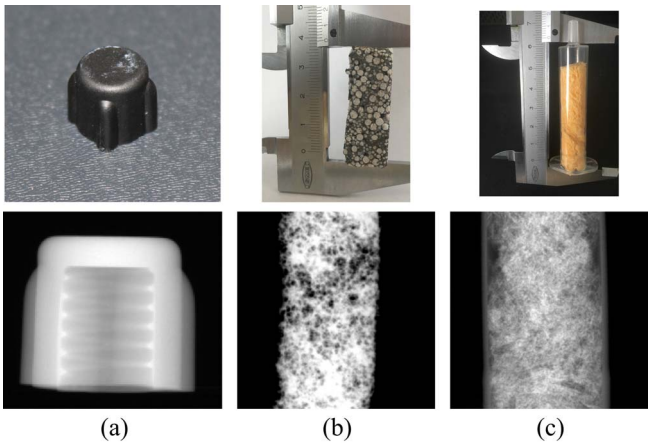

Fig. 9. Top row: pictures of the imaged objects. Bottom row: one projection of each object. (a) Glue cap. (b) Concrete sample. (c) Sponge sample.

TABLE II
CALIBRATION USING DIFFERENT SUBSETS Ω OF PROJECTIONS

	η in deg.	θ in deg.	ϕ in deg.	u_0 in mm.	v_0 in mm.
DCC-based #1	0.9301	0.2032	-0.1107	-0.0016	0.2912
DCC-based #2	0.926	0.2198	-0.1091	-0.0013	0.2754
DCC-based #3	0.9092	0.2439	-0.104	-0.0024	0.2846
DCC-based #4	0.8844	0.2476	-0.1061	-0.0047	0.2997
DCC-based #5	0.8567	0.2406	-0.1137	-0.0087	0.3108
DCC-based #6	0.8542	0.2237	-0.1014	-0.0083	0.26
DCC-based #7	0.8501	0.2075	-0.1099	-0.0025	0.2535
DCC-based #8	0.8485	0.2159	-0.1097	-0.0005	0.3015
SD	0.035	0.017	-0.004	-0.003	0.020

The negative-log transform was then applied so that the projection data correspond to the line-integral model described in (1). We report results on three different datasets: the first one is the projection data of the plastic cap from a tube of glue, approximately 1 cm wide. The rotating support platform was in the flat-field images and therefore subtracted from the projection of the glue-cap. The glue-cap was small enough to be completely contained in the projections. Consequently, no projections were truncated. The values of R and D were physically measured to be 219 and 295 mm. The second dataset was acquired from a sample of concrete foam. All projections were truncated in the direction of the rotation axis (axial truncation). Measures of R and D were 114 and 137 mm, respectively. For this sample, a 0.4 mm aluminum filter was placed in front of the X-ray tube to harden the X-ray beam to make the projection data better fit the line integral model. The third data consisted in a piece of sponge placed into a plastic syringe. Projections were also axially truncated. Measures of R and D were 195 and 259 mm, respectively. See pictures and sample projections of the three objects in Fig. 9.

B. Reconstruction With Complete Data

The calibration method was applied to the projections acquired from each scan, using the *nominal* geometry as first guess. The output values are indicated in Table II. Each of the eight rows in this table corresponds to a different subset of projections, from which the cost function was computed. The first one was composed of nine equally spaced projections, starting with projections at angle 0. Each subsequent subset was shifted by 5 projections (5°). Fig. 10 shows coronal and transverse slices from the reconstructed images with the *nominal* geometry and compares them to reconstructions with a geometry estimated using an *off-line* marker-based method and our DCC-calibrated geometry. The alignment problem described in Section IV-B was encountered here too and the two calibrated

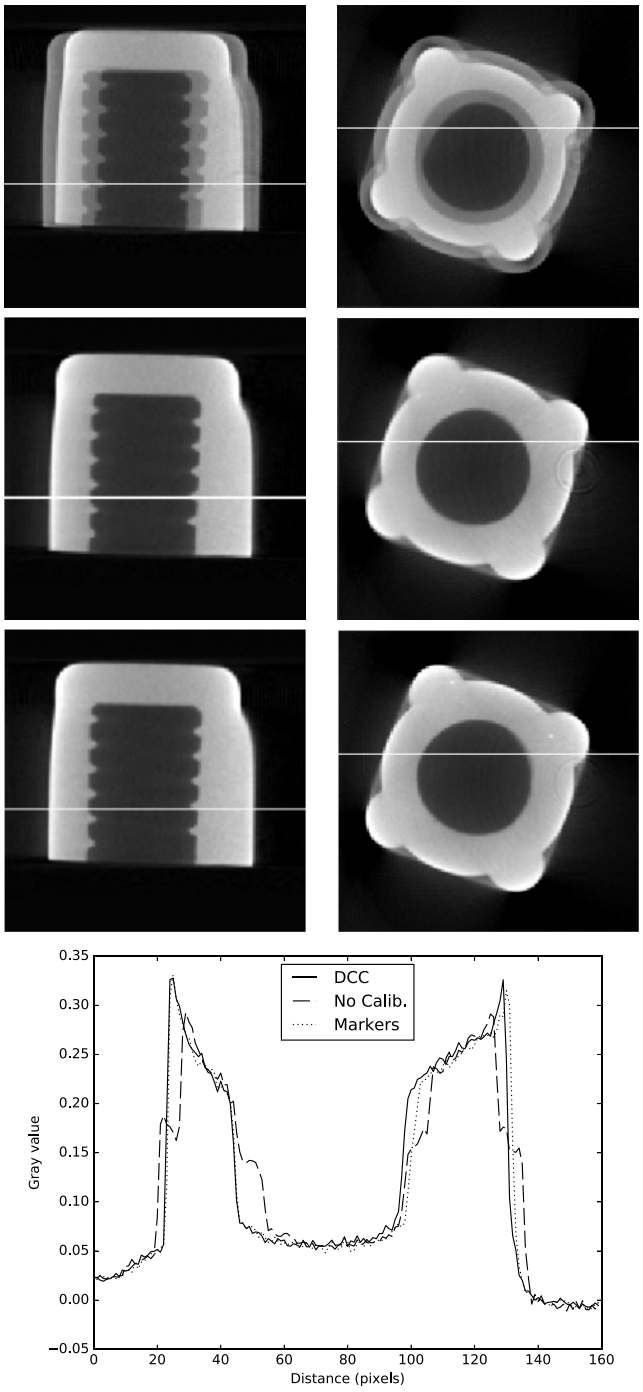

Fig. 10. Coronal (left) and transverse (right) slices of the reconstructed image without calibration (top row), with DCC-based calibration (second row) and with marker-based calibration (third row). The intersection of both slices is represented by the white line. The corresponding intensity profiles are plotted on the bottom figure.

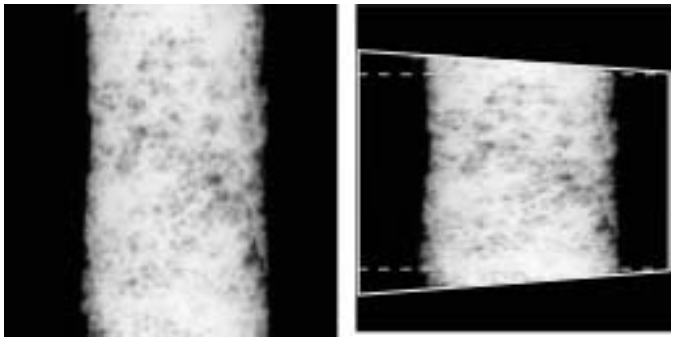

Fig. 11. Axial truncation management: only those rows between the two dashed lines are retained in the virtual projection.

reconstructions were registered manually in the y direction for comparison. Note first that subdegree angular misalignments and submillimeter detector shifts lead to severe artifacts in the reconstruction, especially at the edges of the object (see top-row of Fig. 10). Second, the image quality was significantly improved when reconstruction was computed with the DCC-calibrated geometry. The edges are sharp as illustrated by the profiles in Fig. 10. Of course, the calibration procedure does not correct for other CT artifacts which degrade both uncalibrated and calibrated reconstructed images (e.g., cupping, probably due to beam hardening, and ring artifacts).

C. Reconstruction With Axially Truncated Data

This section explains how our calibration procedure can deal with axially truncated data with application to the truncated data acquired on the same μ-CT system (Fig. 9 middle and right).

1) Handling Axial Truncation: Our cost function is the sum of square differences between integral over rows of the virtual detector. For that reason, truncation in the v-direction does not cause any difficulty as long as there is no truncation in the u-direction. This feature is specific to the nature of the DCCs used in the cost function. In our implementation, care must be taken at the backprojection level because the square physical detector is backprojected to a trapezoidal shape on the virtual detector, with horizontal pixel rows backprojected to oblique pixel rows of varying angle (except for the central line, which remains horizontal). The situation is depicted in Fig. 11. The virtual projection can therefore be limited to those horizontal rows of the virtual detector that are not truncated (rows between the two dashed lines on Fig. 11 right).

2) Results: The calibration procedure was applied to the concrete and the sponge datasets. The nominal geometry served as initial guess. For the concrete sample, the scanning distances R and D were set to 114 and 137 mm, respectively. The resulting cone-angle was approximately 14°. For the sponge sample, $R = 195$ mm and $D = 259$ mm. Axial and transverse slices of the reconstructed volumes are shown in Figs. 12 and 13. In the uncalibrated reconstructions, small structures of the object are barely distinguishable. In the calibrated reconstruction of the concrete sample, though cone-beam and beam-hardening artifacts are still present, the detailed structures (air bubbles in the concrete foam) are much more sharply reconstructed.

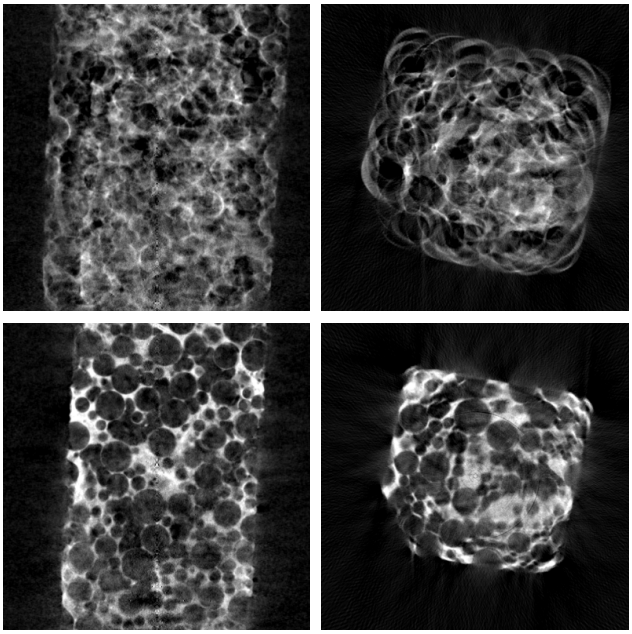

Fig. 12. Concrete sample. Coronal (left) and transverse (right) slices of the reconstructed volume without calibration (top row) and with our DCC-based calibration (bottom row).

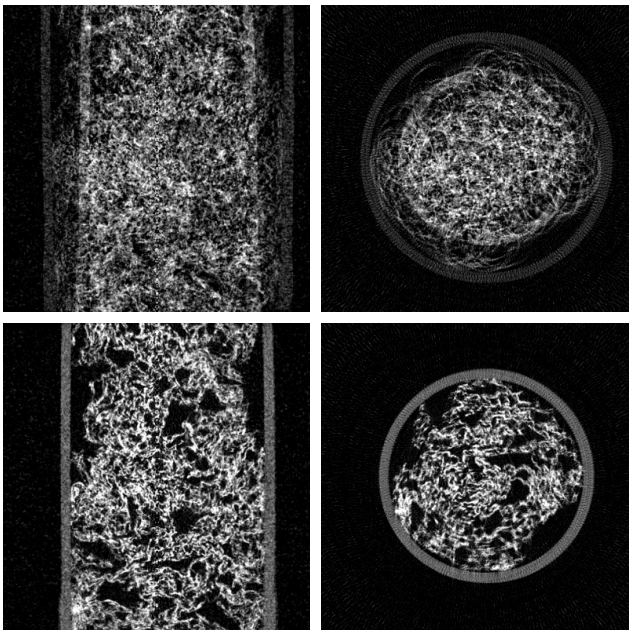

Fig. 13. Sponge sample. Coronal (left) and transverse (right) slices of the reconstructed volume without calibration (top row) and with our DCC-based calibration (bottom row).

VI. Conclusion

We proposed an *on-line* calibration method to estimate five geometric parameters of a μ-CT system. The method is based only on consistency of the "production" scan. It requires no prior (*off-line*) calibration scan. The quality of the reconstructed images in the experiments compares with the robust

"classical" marker-based calibration method. Furthermore, the calibration method can correctly handle axially-truncated data, which is an untypical feature for DCC-based application.

The design of our cost function can probably be refined. A short study on the individual contribution of a pair of projections revealed that pairs angularly separated by more than 90° contributed more than close pairs. Hence, a cost function built from such pairs may convey more independent information and hence lead to more robust estimation. Another question is related to the dependency of the cost function on the object. We have carried out some simulations (similar to those in Figs. 6 and 8) on objects with sharp edges (a simplex-like simulated object) or plate-like objects (very small extent in the v-direction). In all cases, the cost function behaved similarly to the Shepp–Logan study, with regards to each individual parameter or with regards to the (θ, v_0) pair. However, the cost function behaved differently when the plate-like object was placed in the central plane (containing the source trajectory). But, in this case, the geometry collapses to fan-beam, with its own geometric parameters (for example, θ plays no role).

The investigation of the interplay between geometric parameters is a possible future direction of research. Fig. 8 reveals that a large error on one parameter can be compensated by a large error on the second in terms of consistency. We are also extending this paper in two directions. The first one applies the same principles to estimate projection-specific calibration parameters, by using a similar cost function for each projection. Second, the comparison of our method with the work in [2], later described as ECCs [3]. ECCs are also applied to pairs of projections and use a similar geometry of lines on the two detectors (as shown in Fig. 5). However, the theoretical foundations are different because the ECCs are based on Grangeat's formula and require the computation of a derivative. Whether these conditions are equivalent to the conditions used in this paper still needs to be understood and is ongoing work.

REFERENCES

[1] M. S. Levine, E. Y. Sidky, and X. Pan, "Consistency conditions for cone-beam CT data acquired with a straight-line source trajectory," *Tsinghua Sci. Technol.*, vol. 15, no. 1, pp. 56–61, Feb. 2010. [Online]. Available: http://www.ncbi.nlm.nih.gov/pmc/articles/PMC2886312/

[2] C. Debbeler, N. Maass, M. Elter, F. Dennerlein, and T. M. Buzug, "A new CT rawdata redundancy measure applied to automated misalignment correction," in *Proc. 12th Int. Meeting Fully Three Dimensional Image Reconstruct. Radiol. Nucl. Med.*, 2013, pp. 264–267. [Online]. Available: http://www.fully3d.org/2013/Fully3D2013Proceedings.pdf

[3] A. Aichert *et al.*, "Epipolar consistency in transmission imaging," *IEEE Trans. Med. Imag.*, vol. 34, no. 11, pp. 2205–2219, Nov. 2015.

[4] F. Noo, R. Clackdoyle, C. Mennessier, T. A. White, and T. J. Roney, "Analytic method based on identification of ellipse parameters for scanner calibration in cone-beam tomography," *Phys. Med. Biol.*, vol. 45, no. 11, pp. 3489–3508, 2000. [Online]. Available: http://stacks.iop.org/0031-9155/45/i=11/a=327

[5] M. J. Daly, J. H. Siewerdsen, Y. B. Cho, D. A. Jaffray, and J. C. Irish, "Geometric calibration of a mobile C-arm for intraoperative cone-beam CT," *Med. Phys.*, vol. 35, no. 5, pp. 2124–2136, May 2008.

[6] L. von Smekal, M. Kachelriess, E. Stepina, and W. A. Kalender, "Geometric misalignment and calibration in cone-beam tomography," *Med. Phys.*, vol. 31, no. 12, pp. 3242–3266, Dec. 2004.

[7] R. Hartley and A. Zisserman, *Multiple View Geometry in Computer Vision*, 2nd ed. Cambridge, U.K.: Cambridge Univ. Press, 2000.

[8] G. T. Gullberg, B. M. Tsui, C. R. Crawford, J. G. Ballard, and J. T. Hagius, "Estimation of geometrical parameters and collimator evaluation for cone beam tomography," *Med. Phys.*, vol. 17, no. 2, pp. 264–272, 1990. [Online]. Available: http://dx.doi.org/10.1118/1.596505

[9] P. Rizo, P. Grangeat, and R. Guillemaud, "Geometric calibration method for multiple-head cone-beam SPECT system," *IEEE Trans. Nucl. Sci.*, vol. 41, no. 6, pp. 2748–2757, Dec. 1994.

[10] Y. Cho, D. J. Moseley, J. H. Siewerdsen, and D. A. Jaffray, "Accurate technique for complete geometric calibration of cone-beam computed tomography systems," *Med. Phys.*, vol. 32, no. 4, pp. 968–983, Apr. 2005.

[11] K. Yang, A. L. C. Kwan, D. F. Miller, and J. M. Boone, "A geometric calibration method for cone beam CT systems," *Med. Phys.*, vol. 33, no. 6, pp. 1695–1706, Jun. 2006.

[12] C. Mennessier, R. Clackdoyle, and F. Noo, "Direct determination of geometric alignment parameters for cone-beam scanners," *Phys. Med. Biol.*, vol. 54, no. 6, pp. 1633–1660, 2009. [Online]. Available: http://stacks.iop.org/0031-9155/54/i=6/a=016

[13] Y. Kyriakou, R. M. Lapp, L. Hillebrand, D. Ertel, and W. A. Kalender, "Simultaneous misalignment correction for approximate circular cone-beam computed tomography," *Phys. Med. Biol.*, vol. 53, no. 22, pp. 6267–6289, Oct. 2008. [Online]. Available: http://dx.doi.org/10.1088/0031-9155/53/22/001

[14] A. Kingston, A. Sakellariou, T. Varslot, G. Myers, and A. Sheppard, "Reliable automatic alignment of tomographic projection data by passive auto-focus," *Med. Phys.*, vol. 38, no. 9, pp. 4934–4945, 2011.

[15] J. Muders and J. Hesser, "Stable and robust geometric self-calibration for cone-beam CT using mutual information," *IEEE Trans. Nucl. Sci.*, vol. 61, no. 1, pp. 202–217, Feb. 2014.

[16] S. Ouadah, J. W. Stayman, G. J. Gang, T. Ehtiati, and J. H. Siewerdsen, "Self-calibration of cone-beam CT geometry using 3D–2D image registration," *Phys. Med. Biol.*, vol. 61, no. 7, pp. 2613–2632, 2016. [Online]. Available: http://stacks.iop.org/0031-9155/61/i=7/a=2613

[17] S. Basu and Y. Bresler, "Uniqueness of tomography with unknown view angles," *IEEE Trans. Image Process.*, vol. 9, no. 6, pp. 1094–1106, Jun. 2000.

[18] S. Basu and Y. Bresler, "Feasibility of tomography with unknown view angles," *IEEE Trans. Image Process.*, vol. 9, no. 6, pp. 1107–1122, Jun. 2000.

[19] D. Panetta, N. Belcari, A. D. Guerra, and S. Moehrs, "An optimization-based method for geometrical calibration in cone-beam CT without dedicated phantoms," *Phys. Med. Biol.*, vol. 53, no. 14, pp. 3841–3861, 2008. [Online]. Available: http://stacks.iop.org/0031-9155/53/i=14/a=009

[20] Y. Meng, H. Gong, and X. Yang, "Online geometric calibration of cone-beam computed tomography for arbitrary imaging objects," *IEEE Trans. Med. Imag.*, vol. 32, no. 2, pp. 278–288, Feb. 2013.

[21] V. Patel *et al.*, "Self-calibration of a cone-beam micro-CT system," *Med. Phys.*, vol. 36, no. 1, pp. 48–58, Jan. 2009.

[22] N. Maass, F. Dennerlein, A. Aichert, and A. Maier, "Geometrical jitter correction in computed tomography," in *Proc. 3rd Int. Conf. Image Formation X-Ray Comput. Tomograph.*, Salt Lake City, UT, USA, 2014, pp. 338–342.

[23] R. Frysch and G. Rose, "Rigid motion compensation in interventional C-arm CT using consistency measure on projection data," in *Proc. 18th Int. Conf. Med. Image Comput. Comput. Assisted Interventions*, Munich, Germany, 2015, pp. 298–306.

[24] R. Clackdoyle, S. Rit, Y. Hoscovec, and L. Desbat, "Fanbeam data consistency conditions for applications to motion detection," in *Proc. 3rd Int. Conf. Image Formation X-Ray Comput. Tomograph.*, 2014, pp. 324–328.

[25] H. Yu, Y. Wei, J. Hsieh, and G. Wang, "Data consistency based translational motion artifact reduction in fan-beam CT," *IEEE Trans. Med. Imag.*, vol. 25, no. 6, pp. 792–803, Jun. 2006.

[26] S. Tang *et al.*, "Data consistency condition–based beam-hardening correction," *Opt. Eng.*, vol. 50, no. 7, 2011, Art. no. 076501.

[27] S. Helgason, *The Radon Transform* (Progress in Mathematics). Boston, MA, USA: Birkhäuser, 1999. [Online]. Available: http://opac.inria.fr/record=b1095821

[28] D. Ludwig, "The radon transform on Euclidean space," *Commun. Pure Appl. Math.*, vol. 19, no. 1, pp. 49–81, 1966. [Online]. Available: http://dx.doi.org/10.1002/cpa.3160190105

[29] F. Natterer, *The Mathematics of Computerized Tomography* (Classics in Applied Mathematics). Philadelphia, PA, USA: Soc. Ind. Appl. Math., 2001. [Online]. Available: https://books.google.fr/books?id=pZMdcI0WZxcC

[30] S. R. Deans, *The Radon Transform and Some of Its Applications*. Mineola, NY, USA: Dover, 1993.

[31] R. Clackdoyle, "Necessary and sufficient consistency conditions for fan-beam projections along a line," *IEEE Trans. Nucl. Sci.*, vol. 60, no. 3, pp. 1560–1569, Jun. 2013.

[32] D. V. Finch and D. C. Solmon, "Sums of homogeneous functions and the range of the divergent beam X-ray transform," *Numer. Funct. Anal. Optim.*, vol. 5, no. 4, pp. 363–419, 1983.

[33] F. Noo, M. Defrise, R. Clackdoyle, and H. Kudo, "Image reconstruction from fan-beam projections on less than a short scan," *Phys. Med. Biol.*, vol. 47, no. 14, pp. 2525–2546, 2002. [Online]. Available: http://stacks.iop.org/0031-9155/47/i=14/a=311

[34] G.-H. Chen and S. Leng, "A new data consistency condition for fan-beam projection data," *Med. Phys.*, vol. 32, no. 4, pp. 961–967, 2005. [Online]. Available: http://scitation.aip.org/content/aapm/journal/medphys/32/4/10.1118/1.1861395

[35] Y. Wei, H. Yu, and G. Wang, "Integral invariants for computed tomography," *IEEE Signal Process. Lett.*, vol. 13, no. 9, pp. 549–552, Sep. 2006.

[36] S. Tang, Q. Xu, X. Mou, and X. Tang, "The mathematical equivalence of consistency conditions in the divergent-beam computed tomography," *J. X-Ray Sci. Technol.*, vol. 20, no. 1, pp. 45–68, 2012.

[37] S. Rit *et al.*, "The reconstruction toolkit (RTK), an open-source cone-beam CT reconstruction toolkit based on the insight toolkit (ITK)," *J. Phys.*, vol. 489, no. 1, 2014, Art. no. 012079. [Online]. Available: http://stacks.iop.org/1742-6596/489/i=1/a=012079

[38] L. A. Feldkamp, L. C. Davis, and J. W. Kress, "Practical cone-beam algorithm," *J. Opt. Soc. Amer. A, Opt. Image Sci.*, vol. 1, no. 6, pp. 612–619, Jun. 1984. [Online]. Available: http://josaa.osa.org/abstract.cfm?URI=josaa-1-6-612

[39] A. Kak and M. Slaney, *Principles of Computerized Tomographic Imaging*. Philadelphia, PA, USA: Soc. Ind. Appl. Math., 2001. [Online]. Available: http://epubs.siam.org/doi/abs/10.1137/1.9780898719277

[40] M. J. D. Powell, "An efficient method for finding the minimum of a function of several variables without calculating derivatives," *Comput. J.*, vol. 7, no. 2, pp. 155–162, 1964.